# Airborne wind energy system test bench electrical emulator

Carolina Nicolás-Martín <sup>1</sup>, David Santos-Martín <sup>1</sup>, Francisco DeLosRíos-Navarrete <sup>2,3</sup>, and Jorge González-García <sup>2</sup>

**Correspondence:** Carolina Nicolás-Martín (canicola@ing.uc3m.es)

#### Abstract.

Airborne Wind Energy Systems (AWES) offer a promising alternative to conventional wind turbinesroute to high-altitude wind harvesting, but their commercialization is hindered by challenges in efficiently converting the highly dynamic mechanical power of tethered flight remains limited by the challenge of converting highly dynamic tethered flight power into stable electrical energy. While extensive most research has focused on optimizing AWES flight trajectories and controlstrategies, the power conversion stage, which is critical for integrating AWES into electrical grids, is relatively under-researched. To bridge this gap, reliable and flexible electrical test bench emulators are needed to replicate AWES dynamics under controlled conditions, enabling systematic evaluation and optimization of power electronics and control strategies.

This paper presents—, the mechanical-to-electrical conversion stage requires further experimental validation. This paper introduces a validated electrical test bench emulator and a torque<del>ripple-optimized</del>—ripple-optimized Model Predictive Control (MPC) strategy<del>designed to enhance the performance of AWES ground station generators. The proposed emulator accurately reproduces the mechanical-electrical interactions of a real AWES by simulating the—, evaluated using two real AWES flight datasets.</del>

The emulator reproduces variable tether forces and reeling dynamics encountered during optimal under optimal figure-8 crosswind flight. Two electrical topologies are introducedDC-bus topologies are compared: a separated DC bus configuration that closely mimics real AWES energy storage dynamics bus that accurately mimics AWES storage dynamics (≈98% fidelity) but demands 45–55% more battery capacity, and a common DC bus topology that minimizes battery requirements for extended control testing, bus that recirculates energy, reducing storage needs by two-thirds. When realistic storage dynamic emulation is required, the separated bus configuration is the only suitable option. The proposed MPC strategy ensures precise generator speed and torque regulation, achieving less than 1% root mean square torque-tracking root mean squared error (RMSE) in torque tracking while optimizing energy efficiencybelow 0.11% (Dataset 1) and 0.14% (Dataset 2), and speed-tracking RMSEs of 0.44% and 0.82%, respectively.

Using experimental flight data, the test bench demonstrates an overall energy efficiency exceeding 80% and peak conversion efficiencies up to Overall energy efficiencies reach 82% with Dataset 1 and 60% with Dataset 2, with peak instantaneous efficiencies reach 82% with Dataset 1 and 60% with Dataset 2, with peak instantaneous efficiencies reach 82% with Dataset 1 and 60% with Dataset 2, with peak instantaneous efficiencies reach 82% with Dataset 1 and 60% with Dataset 2, with peak instantaneous efficiencies reach 82% with Dataset 1 and 60% with Dataset 2, with peak instantaneous efficiencies reach 82% with Dataset 1 and 60% with Dataset 2, with peak instantaneous efficiencies reach 82% with Dataset 1 and 60% with Dataset 2.

<sup>&</sup>lt;sup>1</sup>Department of Electrical Engineering, Universidad Carlos III de Madrid, Avenida de la Universidad 30, 28911 Leganés (Madrid), Spain

<sup>&</sup>lt;sup>2</sup>Department of Aerospace Engineering, Universidad Carlos III de Madrid, Avenida de la Universidad 30, 28911 Leganés (Madrid), Spain

<sup>&</sup>lt;sup>3</sup>CT Ingenieros A.A.I. S.L. Avenida Leonardo Da Vinci 22, 28050 Getafe (Madrid), Spain

25 ficiencies of 93%, with and 88%. Permanent Magnet Synchronous Generators (PMSG) outperforming outperform Induction Machines (IM) by 4% in Dataset 1 and up to 20% in Dataset 2–6% in instantaneous efficiency. These findings, with instantaneous gains of 2–10% at high power. Off-nominal operation degrades cycle efficiency and drives higher battery cycling even in a common-bus setup, highlighting the importance of correct machine dimensioning. However, when storage dynamics are not under study, the common-bus configuration is the most cost-effective option, requiring less hardware and imposing lower peak discharge stresses.

These results establish electrical test benches as essential for AWES development, offering a scalable platform for optimizing power conversionand control, which advances AWES as a viable renewable energy technology.

bench emulators as essential platforms for systematic evaluation and optimization of AWES power conversion, informing both machine design and control strategies for scalable, efficient AWES deployment.

## 1 Introduction

35

Airborne Wind Energy Systems (AWES) are an innovative renewable energy technology designed to harvest high-altitude winds using autonomous, tethered aircraft. These systems offer access to stronger and more consistent wind resources than those available at lower altitudes, leading to improved capacity factors and higher energy yields (?). Additionally, unlike traditional horizontal-axis wind turbines, AWES eliminate the need for large, static support structures, reducing construction costs and minimizing environmental impacts (?).

Since their initial conceptualization in the 1980s (?), AWES have undergone significant development. Over the past two decades, researchers have proposed a variety of system architectures, ranging from small-scale prototypes (?????) to precommercial systems with rated power capacities of up to 200 kW (??). These systems are commonly classified based on the location of energy conversion: onboard the aircraft via wind turbines or on the ground using the traction forces exerted on the tether to drive a generator. Ground-generation AWES, which are the focus of this study, typically operate in a pumping cycle consisting of two phases: the traction (reel-out) phase, where energy is generated as the aircraft flies crosswind, and the retraction (reel-in) phase, where the aircraft is reeled back at an angle that ensures minimal energy consumption.

Over the past decades, AWES have witnessed remarkable advancements in aerodynamic design and control, with numerous studies optimizing tethered aircraft trajectories, lift-to-drag ratios, and energy harvesting strategies (?). These developments have enabled AWES to reach high operational efficiency, making them a promising alternative to traditional wind energy technologies. However, while aerodynamic aspects of AWES have matured significantly, the electrical power conversion systems required for ground-generation remain relatively underexplored.

AWES operate in a highly dynamic environment where mechanical power generation fluctuates due to variations in wind conditions, flight trajectories, and tether forces (?). To effectively harness and stabilize this intermittent energy, robust electrical systems and advanced control strategies are crucial. Despite extensive optimization of mechanical power extraction, research on power conversion in AWES ground stations remains limited. As AWES move toward commercialization, addressing challenges

such as energy storage optimization, fault tolerance, and reactive power control is essential to ensure reliable and scalable operation.

Existing studies (??) have made notable contributions by proposing power conversion topologies and control strategies, including optimal damping (?) and cascade control approaches for induction generators (?). Nevertheless, many of these approaches would benefit from experimental validation that incorporates AWES-specific flight data. For larger-scale systems, ? proposed a multi-machine AWES park using permanent magnet synchronous generators, with later studies (??) exploring a direct AC bus connection for offshore applications. While reducing reliance on converters, this approach raises challenges in reactive power and tether torque control. Very advanced power converter control techniques have been explored by ? and ? for AWES applications. Both strategies showing an enhancement on control performance, although validation under AWES-specific conditions is still needed. Research on machine selection and energy storage has identified electrically excited synchronous machines and permanent magnet synchronous machines with high-energy magnets as promising candidates (?). Studies on power electronics (?) and energy storage (??) highlight battery storage as a viable option for power smoothing, considering its efficiency and cost-effectiveness compared to alternatives.

Significant further research is required to complement these valuable first contributions and experimental validation is key to refining AWES power conversion. Electrical test bench emulators offer a crucial tool in bridging the gap between aerodynamic advancements and electrical system maturity. By accurately replicating AWES flight conditions in a controlled environment, these emulators allow for in-depth analysis, optimization, and validation of power conversion architectures before large-scale deployment. They enable researchers to evaluate system efficiency, investigate new control methodologies, and assess the impact of various energy storage and grid-integration strategies. Previous work has contributed significantly to the development of laboratory-scale test bench emulators for AWES. For instance, ? introduced a real-time emulator utilizing a Permanent Magnet Synchronous Generator (PMSG) with field-oriented control techniques, providing valuable insights into the emulation of airborne wind turbine dynamics. While this study advances emulator-based AWES research, further exploration is needed to assess alternative control strategies tailored to the specific challenges of AWES applications. Additionally, incorporating energy storage dynamics and alternative machine topologies could enhance the versatility and applicability of test bench emulators. Addressing these aspects, along with control approaches aimed at minimizing torque ripple, would contribute to more comprehensive and high-fidelity AWES emulation.

In response to these challenges, the study detailed in this article develops and validates a scalable, fully electrical test bench emulator for AWES ground-generation systems. The emulator is designed to replicate the dynamic behavior of real-world AWES during both reel-in-

#### 1.1 Novelty, scope and limitations

Existing AWES test-bench emulators typically focus on a single machine type and a single DC-bus topology, without evaluating how these choices impact dynamic emulation fidelity. For example, Kumar et al. present a PMSG-only emulator with one fixed DC-bus arrangement and field-oriented control?, but do not compare alternative machines or storage interconnections.

Key novel contributions:

90

70

- 1. Dual-machine comparison under realistic AWES cycles. Both a permanent-magnet synchronous machine and reel-out phases. Two battery connection topologies are explored: one with separate DC busesfor the generating and emulating sides, and another with a an induction machine are evaluated using real flight tether-force and reel-speed data from two publicly available datasets (Aruba and Leiden). This allows assessment of how machine choice affects torque tracking, efficiency, and ripple performance under identical AWES dynamics.
- 2. Two DC-bus configurations. Unlike prior work that adopts a single storage topology, two configurations are implemented and compared:
  - separated DC buses: two independent DC-DC converters and batteries to emulate both charge and discharge dynamics,
  - common DC busto facilitate efficient : a single DC-DC stage enabling direct energy recirculation. A Model
     Predictive Control

The separated bus topology is suited for tests requiring realistic storage charge—discharge behavior, while the common bus is suited for tests focused soley on machine dynamics and repeated operation with minimal battery cycling.

3. Ripple-optimized model predictive control (MPC) scheme with a ripple optimization strategy is employed to ensure precise control and minimize torque ripple. Using experimental tether force and length profiles (?), the emulator is evaluated for its control performance, energy storageefficiency, and applicability to long-term dynamic testing. for torque-ripple minimization. The control strategy explicitly considers the dynamic demands of AWES operation by selecting a model predictive control scheme that offers improved dynamic response while actively reducing torque ripple, which is critical for preserving drivetrain components. A three-state sequence (S<sub>i</sub>, S<sub>0</sub>, S<sub>i</sub>) is applied each sampling period to achieve low ripple levels not addressed in previous emulators.

# Scope and limitations:

95

100

115

All results presented in this work are based on detailed numerical simulations in MATLAB/Simulink with Simscape Electrical. A physical test bench has not yet been built, as the focus of this work is on an initial validation stage that supports design decisions for future experimental platforms. By comparing different machine types, DC-bus topologies, and control strategies under identical and well-controlled conditions, the simulation environment enables informed choices on configurations that would be most effective to implement and test in hardware.

The system is represented as follows:

- Electrical machines (PMSG and IM), converters, battery storage, and the model predictive control with ripple-optimization are fully modelled in simulation.
- Torque and reel-in/reel-out speed profiles are derived from experimental AWES flight data recordings, using two publicly available datasets.

Machine parameters, converter ratings, and mechanical relations are based on typical values reported in the literature
and reference texts, adapted to the requirements of this study where specific AWES-oriented data were not available.

This approach provides a rigorous basis for guiding the design of future physical test benches while enabling a comprehensive evaluation of emulator behavior in a controlled environment. The absence of experimental implementation and validation is acknowledged as a current limitation of this study and is identified as a key priority for future work.

The remainder of this paper is structured as follows: Section 2 presents the proposed emulator topology and control strategies. Section 3 describes the validation methodology using measured AWES flight data. Section 4 discusses the results and their implications for AWES power conversion systems. Finally, Sect. 5 concludes with key findings and recommendations for future work.

# 2 Methodology

130

135

140

150

This section outlines the methodology used to develop and validate the proposed AWES test-bench emulator. The emulator is designed to replicate the dynamic behavior of a real AWES during the reel-in and reel-out phases. It begins by describing the reel-in and reel-out phases. Fig. 1 provides an overview of the workflow, starting with the definition of the AWES electrical power conversion system and the emulator structure, detailing the interaction between and the modeling of key components such as the generator, emulator machine, power converters, and energy storagesystem. Next,. It then incorporates experimental flight data to derive torque and speed profiles, applies a ripple-optimized model predictive control strategy, and implements the resulting configurations in a Simulink/Simscape environment. Within this methodology section, these steps are presented in detail: first, the generic AWES electrical power conversion system and emulator structure; next, the aerodynamic system inputs for AWES power conversion are introduced, defining the key flight and mechanical parameters that influence emulator operationaerodynamic inputs and reference profile generation; then, the two proposed electrical topologies; and finally, the control strategy and discretization approach. Both induction machines and permanent magnet synchronous generators are evaluated under separated and common DC-bus topologies, with performance compared in terms of speed tracking, torque fidelity, efficiency, and storage behavior.

# 145 2.1 AWES electrical power conversion system and emulator structure

Publicly available, detailed information on specific topologies for mechanical-to-electrical conversion in ground-based airborne wind energy (AWE) systems remains scarce, to the best of the authors' knowledge. This is followed by a discussion of two electrical topologies for energy conversionand storage, evaluating their suitability for different testing scenarios. Finally, the model predictive control strategy is presented, including its ripple optimization approach and system discretization process largely due to the fact that most existing prototypes are still in a pre-commercial phase. Nevertheless, both academic literature such as ??? and available industrial reports such as ?? consistently indicate that an electrical three-phase machine controlled by a power converter is typically employed for the mechanical-to-electrical conversion. Furthermore, the alternating load patterns arising from the reel-in and reel-out phases make direct grid connection particularly challenging. This underlines the need for an

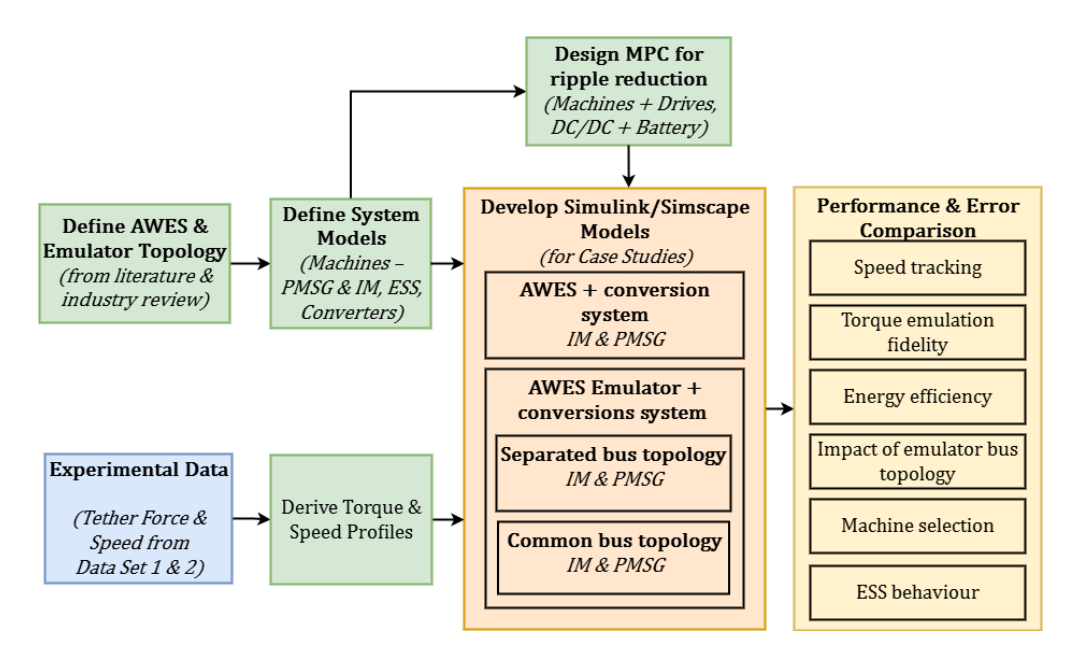


**Figure 1.** Overview of the methodology, showing the workflow from system definition and data processing to simulation and performance evaluation.

energy storage system to smooth power fluctuations and ensure a steady electrical output ??. This requirement is corroborated by the limited industrial disclosures from leading AWES developers—such as Skysails, KitePower, and Kitemill—which report the use of DC battery storage in their systems. Drawing on this information, Figure 2 presents a generalized representation of the most common power conversion process in a ground-station AWES.

# 2.2 AWES electrical power conversion system and emulator structure

Figure-Fig. 2 illustrates the power conversion process in an AWES, control components are represented in color green for clarity. To optimize mechanical power extraction in an AWES, an electrical machine (G) regulates the kite's reeling speed,  $v_{tether}$ , via a DC-AC power converter, ensuring consistent rotation, despite varying tether forces. During the reel-out phase, G operates as a generator, converting mechanical to electrical energy, which is transferred to a high-voltage DC bus. During the reel-in phase, G operates as a motor, spinning in the opposite direction and allowing the tether to retract. A bi-directional DC-DC converter stabilizes the bus voltage by charging a storage device (e.g., a battery) during the reel-out phase and discharging it during the reel-in phase when G functions as a motor to retract the kite. This process ensures efficient energy management and stable system operation during both phases of the AWES cycle. This topology supports both connection to an external AC grid and islanded operation.

Schematic representation of the power conversion process in AWES, including the AWES emulator, energy conversion system, and control interactions.

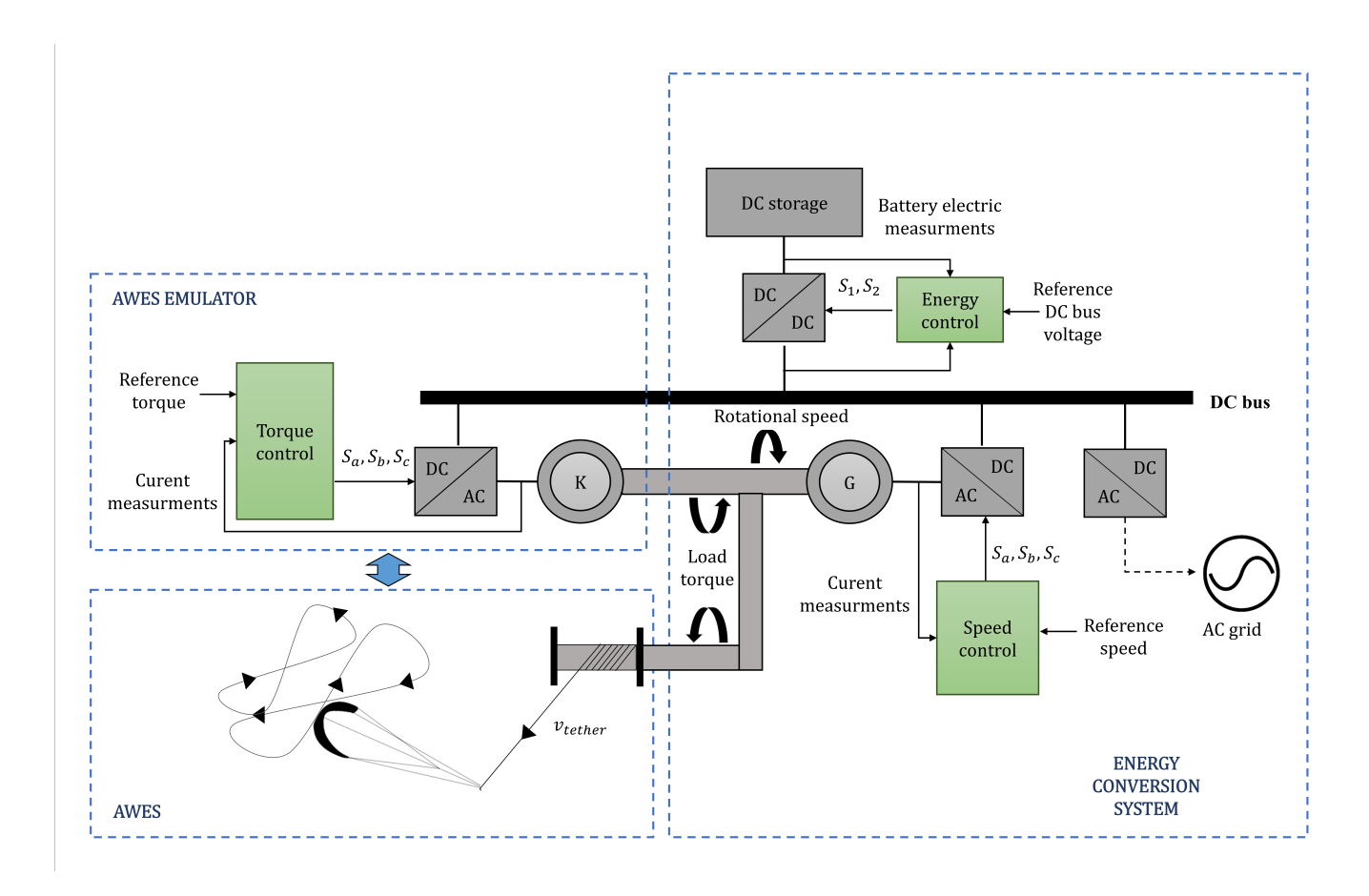


**Figure 2.** Schematic representation of the power conversion process in AWES, including the AWES emulator, energy conversion system, and control interactions.

The proposed AWES emulator simulates the effect of the changing tether forces on the electric machine shaft using another electrical machine (K) that regulates the shaft load torque via a DC-AC power converter. Precise and robust control of this converter is essential to accurately replicate the kite's mechanical behavior.

#### 2.2 Aerodynamic inputs for AWES power conversion

To maximize mechanical power output during the traction phase of the cycle, an AWES aircraft must follow a closed trajectory in crosswind conditions (?). Commonly used flight paths include circular and lemniscate (figure-eight) patterns, with the latter offering more consistent tether forces,  $F_{\text{tether}}$ , which are advantageous for power generation (?) and for grid integration (?). Along this path, tether forces increase during downward turns and decrease during climbing segments due to variations in apparent wind velocity caused by gravity.

The efficiency of mechanical power generation depends on the reeling factor f, which is defined as

180 
$$f = \frac{v_{\text{tether}}}{v_{\text{wind}}},$$
 (1)

where  $v_{\text{tether}}$  is the tether reel-out speed and  $v_{\text{wind}}$  is the wind speed at the wing. The optimal reeling factor,  $f_{\text{opt}}$ , for straight tethers is given by (?)

$$f_{\text{opt}} = \frac{1}{3}\sin\theta\cos\phi,\tag{2}$$

where  $\theta$  and  $\phi$  are the azimuth and elevation angles of the kite respectively. These variables are used to calculate the reference torque,  $T_{\rm load}$ , and rotational speed,  $\omega_m$ , for the emulator, which are defined as

$$T_{\text{load}} = F_{\text{tether}} \cdot R_{\text{drum}} \cdot i, \quad \omega_m = \frac{v_{\text{tether}}}{R_{\text{drum}} \cdot i}, \quad i = \frac{\omega_{drum}}{\omega_m}$$
 (3)

where  $R_{\text{drum}}$  is the drum radius and i is the overall gear ratio of the system's drivetrain. For the sake of simplicity,  $R_{\text{drum}}$  is assumed constant and a value of i = 1 is considered for this study.

To better understand how these variables influence the operation of the electrical power conversion system and kite emulator, Fig. 3 illustrates the distribution of time spent at each combination of angular speed and torque values  $(T_{load}, \omega_m)$  during a reference AWES cycle from ?. The reel-out phase, during which the tether is extended and mechanical power is converted into electrical energy, is characterized by a wide range of operating points. Conversely, in the reel-in phase, where the tether is retracted and energy is consumed to pull the kite back, the torque values exhibit lower variability, and the electrical machine operates as a motor rather than a generator.

#### 2.3 Electric topology for an airborne wind energy system and its test bench emulator

Building on the generalized scheme shown in Fig. 2, in this work we propose a specific implementation for both the AWES ground station and its test bench emulator. The proposed configuration employs a DC battery as the energy storage element, a two-level three-phase DC-AC converter as the machine drive, and a bidirectional DC-DC converter to interface the battery with the DC bus. For the purposes of this study, the system is operated in islanded mode, without connection to an external AC grid.

The electric topology is fundamental for replicating the energy conversion dynamics of an AWES and enabling efficient power flow in the proposed test bench emulator. This section describes the topology for a real AWES and the two emulator configurations designed to simulate its behavior.

# 2.3.1 Topology for an airborne wind energy system

195

200

As shown in Fig. ??4 (a), the proposed topology for a real AWES uses a kite tether wound around a drum connected to a three-phase electrical machine (G). During the reel-out phase, machine G acts as a generator, converting the kite's mechanical energy into electrical energy. During the reel-in phase, it operates as a motor, consuming energy to retract the tether.

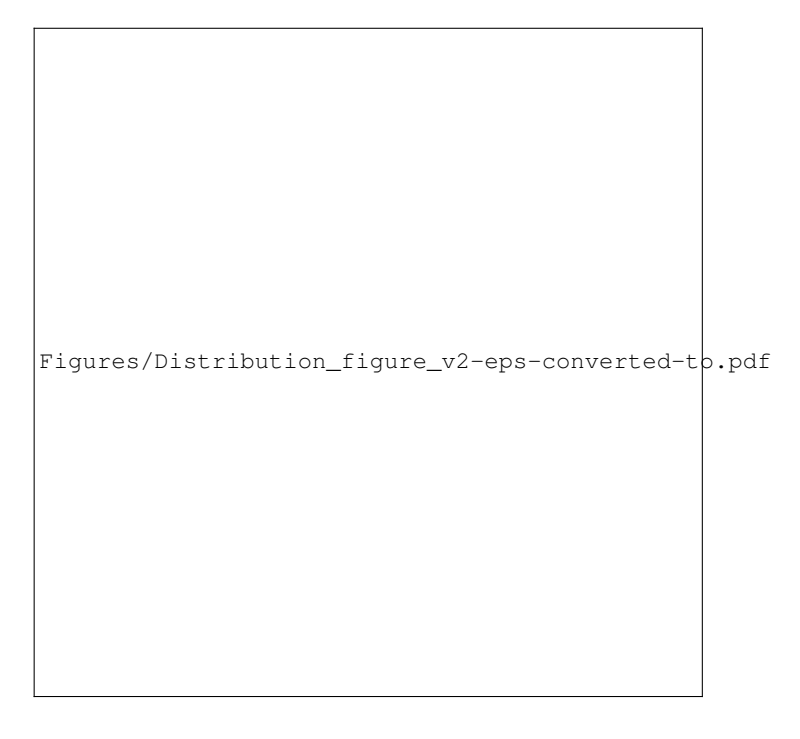


**Figure 3.** Distribution of time spent at each combination of angular speed and torque during the AWES cycle, highlighting the operational differences between the reel-out (generation) and reel-in (motor operation) phases.

Machine G is controlled by a DC-AC converter (G-C-AC) to manage power flow, while the generated energy is stored in a battery (G-B) via a DC-DC converter (G-C-DC). The system's power generation and consumption are governed by the kite's flight dynamics, which dictate the torque applied to the drum.

#### 2.3.2 Proposed emulator topologies

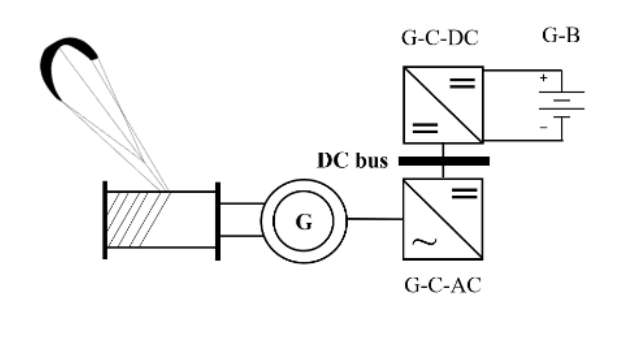
215

220

The AWES test bench emulator simulates the interaction between the kite and the generator using an additional three-phase electrical machine (K), mechanically coupled to machine G. Machine K operates in opposition to G, acting as a motor during the reel-out phase to emulate the kite's mechanical forces, and as a generator during the reel-in phase to recover the mechanical energy applied by G. Two topologies are proposed in Fig. 4 for the emulator, each tailored to specific testing requirements.

The first topology, shown in Fig. ??4 (b), uses two separate DC buses. Machine G connects to its own battery (G-B) through a DC-DC converter (G-C-DC) to store energy generated during the reel-out phase. Similarly, machine K is powered by a separate battery (K-B) through its own DC-DC converter (K-C-DC). This configuration closely replicates the energy storage and flow dynamics of a real AWES, making it ideal for studying energy storage requirements. However, it increases system complexity by requiring two batteries and two DC-DC converters.

The second topology, illustrated in Fig. ??4 (c), simplifies the system by using a common DC bus shared by machines G and K. A single battery (J-B) and a single DC-DC converter (J-C-DC) manage energy storage. During the reel-out phase,



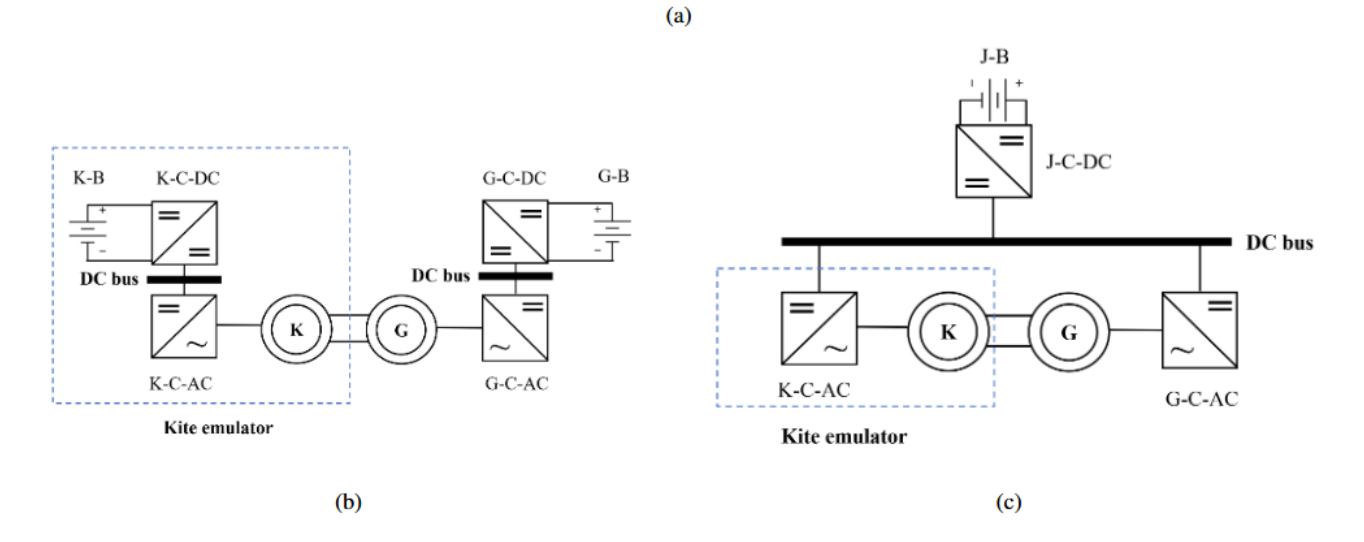


**Figure 4.** Proposed power conversion topologies for the AWES test bench emulator: (a) Proposed power conversion topology for a real AWES, (b) Proposed two-DC bus topology approach for AWES electrical emulator, (c) Proposed common DC bus topology approach for AWES electrical emulator.

Proposed two-DC bus topology approach for AWES electrical emulator. Proposed common DC bus topology approach for AWES electrical emulator.

Proposed power conversion topologies for the AWES test bench emulator.

energy generated by G is recirculated directly to K, reducing battery usage. This topology is more efficient and cost-effective, particularly for extended tests, but it sacrifices accuracy in emulating the distinct energy storage dynamics of a real AWES.

## 225 2.4 Model predictive control strategy

230

235

The control scheme for the power converters is designed to address the dynamic and multi-variable nature of AWES. Compared to conventional wind energy systems, AWES are characterized by lower inertia, exposure to higher and more unpredictable wind conditions, and a highly variable flight cycle profile. These unique features demand a control strategy capable of rapid adjustments and robust performance under changing operating conditions.

MPC was selected for its capability to manage constraints, non-linearities, and fast-changing dynamics. Its excellent steady-state performance and rapid dynamic response make it particularly well-suited for AWES applications, where precise regulation of torque and energy flow is critical (??). In addition, extensive benchmarking in related high-performance drive applications has shown that MPC can outperform conventional strategies such as field-oriented control (FOC) and direct torque control (DTC) in terms of torque tracking, current ripple, and efficiency (??). These findings from the broader literature provide indirect but strong evidence of MPC's superiority, supporting its use in this study. This section outlines the implementation of MPC for regulating the power converters in the proposed topologies (as shown in Sect. 2.3). Key features include a ripple optimization strategy that minimizes fluctuations in controlled variables, ensuring that the kite emulator accurately reproduces the dynamic torque profile of a real AWES. Figure Fig. 5 illustrates the generalized structure of the MPC applied to a power converter, with specific details on its implementation for each system component provided in subsequent sections.

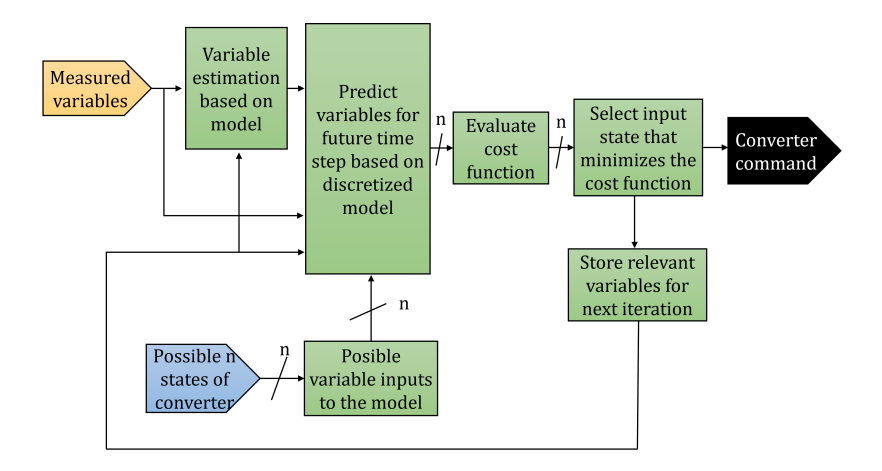


**Figure 5.** General MPC control scheme for power converters.

#### 240 2.4.1 MPC ripple optimization vector strategy

The ripple optimization strategy is a critical enhancement of the proposed MPC, designed to minimize fluctuations in the controlled variables and improve the fidelity of the kite emulator. The MPC algorithm determines the switching states of either

the bi-directional DC-DC converter or the two-level three-phase DC-AC converter. For the DC-DC converter, there are n=2 possible states, while for the DC-AC converter n=7 due to redundant states that produce the same voltage vector (?). The selection of input states directly impacts the system's performance, particularly the accuracy of torque reference tracking and ripple suppression.

Two state selection strategies are evaluated:

245

250

255

270

- Classical  $S_i$  strategy: This conventional approach selects a single optimal state  $S_i$  (e.g.,  $S_0$  to  $S_6$  for the DC-AC converter and  $S_0$  to  $S_1$  for the DC-DC converter) that minimizes the error between the predicted and reference output variables over the entire sampling period  $T_s$ . Once selected, this state remains constant throughout  $T_s$ . While computationally simple, this strategy can lead to higher ripple in the controlled variables, as it does not adjust for intermediate changes within  $T_s$ .
- Symmetrical  $S_i, S_0, S_i$  strategy: This enhanced approach introduces a three-state symmetric input sequence  $(S_i, S_0, S_i)$  to achieve finer control of the output variables. The controller calculates the fraction of  $T_s$  during which  $S_i$  will be applied using a discrete parameter  $f_{\text{duty}}$ , which divides  $T_s$  into three intervals:

$$T_1 = T_3 = \frac{1 - f_{\text{duty}}}{2} T_s,$$
 (4)

$$T_2 = f_{\text{duty}} \cdot T_s. \tag{5}$$

Predefined discrete values for  $f_{\text{duty}}$  are  $\{0,0.2,0.4,0.6,0.8,1\}$ . Unlike the classical strategy, this method predicts the output variables at three points within  $T_s$  ( $T_1$ ,  $T_2$ , and  $T_3$ ), enabling a closer match to the reference values.

The symmetrical  $S_i, S_0, S_i$  strategy provides notable benefits, including reduced ripple in controlled variables, enhanced torque precision, and lower switching frequency. These advantages stem from the inclusion of the intermediate state  $S_0$ , which smooths transitions between  $S_i$  states, as shown in Fig. 6. While this approach incurs a slightly higher computational cost, it is well-supported by modern microcontrollers (?).

The comparison in Fig. 6 highlights the superior performance of the  $S_i, S_0, S_i$  strategy in suppressing ripple and achieving greater accuracy over multiple sampling periods. This optimized strategy plays a vital role in ensuring that the kite emulator accurately replicates the dynamic torque profile of an actual AWES.

## 2.4.2 Model predictive control discretization

The discretization of the system models is essential for implementing MPC. Each component of the system is described in terms of discrete-time equations, enabling the MPC to predict and optimize the control variables. The number of switching states (n), and consequently the number of possible input variables for the model (as shown in Fig. 5), is determined by the type of converter being controlled: n=7 for a two-level three-phase DC-AC converter, which maps to seven distinct stator voltage vectors  $V_s$ , and n=2 for a bi-directional DC-DC converter with two switching states. This section details the discretization process for the induction machine (IM), permanent magnet synchronous generator (PMSG)IM and PMSG, and bi-directional DC-DC converter.

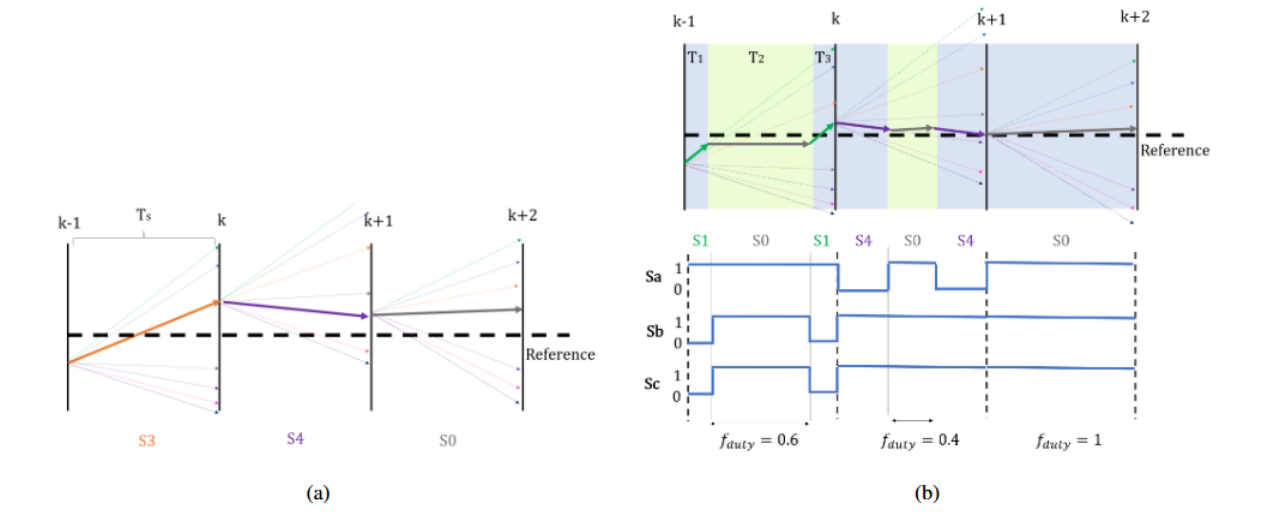


Figure 6. Comparison of MPC input vector strategies for three sample periods: (a) Single input vector  $S_i$  strategy, (b) Symmetrical  $S_i$ ,  $S_0$ ,  $S_i$  input vector strategy.

Symmetrical  $S_i$ ,  $S_0$ ,  $S_i$  input vector strategy. Comparison of MPC input vector strategies for three sample periods.

# 275 Induction Machine

The induction machine's electrical model is expressed in matrix form as follows:

$$\mathbf{v} = \mathbf{A} \cdot \mathbf{s} + \mathbf{B} \cdot \mathbf{r} + \mathbf{C} \cdot \frac{d}{dt} \mathbf{s} + \mathbf{D} \cdot \frac{d}{dt} \mathbf{r}, \tag{6}$$

$$\mathbf{r} = \mathbf{E} \cdot \mathbf{s}.\tag{7}$$

Here,  $\mathbf{v}$ ,  $\mathbf{s}$ , and  $\mathbf{r}$  are vectors containing the system variables, including space vectors for the stator voltage  $\overline{v_s}$ , the stator flux  $\overline{\varphi_s}$ , stator current  $\overline{i_s}$ , rotor flux  $\overline{\varphi_r}$ , and rotor current  $\overline{i_r}$ , as shown in Eq. (8).

The values for matrices A, B, C, and D are provided in Appendix A.

$$\mathbf{v} = \begin{bmatrix} \overline{v_s} \\ 0 \end{bmatrix}, \quad \mathbf{s} = \begin{bmatrix} \overline{\varphi_s} \\ \overline{i_s} \end{bmatrix}, \quad \mathbf{r} = \begin{bmatrix} \overline{\varphi_r} \\ \overline{i_r} \end{bmatrix}. \tag{8}$$

The electromagnetic torque  $T_e$  is computed as

$$T_e = \frac{3}{2} p \operatorname{Im}\{\overline{\varphi_s}^* \cdot \overline{i_s}\},\tag{9}$$

285 where p is the number of pole pairs and  $Im\{...\}$  denotes the imaginary part of a complex number.

The model is discretized using the forward Euler method (?):

$$\mathbf{s}_{k+1} = \mathbf{A}_v \mathbf{v}_k - \mathbf{A}_s \mathbf{s}_k. \tag{10}$$

The matrices  $\mathbf{A}_v$  and  $\mathbf{A}_s$  are calculated as

$$\mathbf{A}_v = (\mathbf{C} + \mathbf{D} \cdot \mathbf{E})^{-1} \cdot T_s,\tag{11}$$

290 
$$\mathbf{A}_s = T_s \cdot (\mathbf{C} + \mathbf{D} \cdot \mathbf{E})^{-1} (\mathbf{A} + \mathbf{B} \cdot \mathbf{E}) - \mathbf{I},$$
 (12)

where  $T_s$  is the sampling time, and **I** is the identity matrix.

# **Permanent Magnet Synchronous Generator**

The PMSG is modeled in the synchronous reference frame as

$$\overline{v_s} = \mathbf{F} \cdot \overline{i_s} + \mathbf{G} \cdot \overline{\varphi_m} + \mathbf{L} \cdot \frac{d}{dt} \overline{i_s}, \tag{13}$$

where  $\overline{v_s}$ ,  $\overline{i_s}$ , and  $\overline{\varphi_m}$  are the space vectors for the stator voltage, stator current, and magnetic flux, respectively, defined as

$$\overline{v_s} = \begin{bmatrix} v_{sd} \\ v_{sq} \end{bmatrix}, \quad \overline{i_s} = \begin{bmatrix} i_{sd} \\ i_{sq} \end{bmatrix}, \quad \overline{\varphi_m} = \begin{bmatrix} \varphi_m \\ 0 \end{bmatrix}.$$
(14)

The values for matrices **F**, **G**, and **L** are provided in Appendix B.

The forward Euler method is applied to discretize the current space vector:

$$\overline{i_{sk+1}} = \mathbf{A}_u \overline{v_{sk}} + \mathbf{A}_i \overline{i_{sk}} - \mathbf{A}_{\varphi_m} \overline{\varphi_{mk}}, \tag{15}$$

300 where the matrices are:

$$\mathbf{A}_{u} = T_{s} \cdot \mathbf{L}^{-1},\tag{16}$$

$$\mathbf{A}_i = \mathbf{I} - T_s \cdot \mathbf{L}^{-1} \cdot \mathbf{F},\tag{17}$$

$$\mathbf{A}_m = -T_s \cdot \mathbf{L}^{-1} \cdot \mathbf{G}. \tag{18}$$

The electromagnetic torque is calculated as

305 
$$T_e = \frac{3}{2}p(i_{sd} \cdot i_{sq} \cdot (L_d - L_q) + \varphi_m \cdot i_{sq}),$$
 (19)

where  $L_d$  and  $L_q$  are the d-axis and q-axis inductances, and  $\varphi_m$  is the permanent magnet flux linkage.

#### **Bi-directional DC-DC converter**

The bi-directional DC-DC converter is modeled as

$$\mathbf{S} \cdot \mathbf{g} = \mathbf{I} \cdot \mathbf{m} + \mathbf{H} \cdot \frac{d}{dt} \mathbf{g},\tag{20}$$

310 where  $\mathbf{g}$  and  $\mathbf{m}$  are vectors defined as

$$\mathbf{g} = \begin{bmatrix} V_{dc} \\ i_L \end{bmatrix}, \quad \mathbf{m} = \begin{bmatrix} V_{bat} \\ I_{dc} \end{bmatrix}. \tag{21}$$

Here,  $V_{dc}$  is the DC bus voltage,  $i_L$  is the inductor current of the converter,  $V_{bat}$  is the battery voltage, and  $I_{dc}$  is the DC bus current.

The matrices S and H are defined as.

315 
$$\mathbf{S} = \begin{bmatrix} s_1 & 0 \\ 0 & s_1 \end{bmatrix}, \quad \mathbf{H} = \begin{bmatrix} 0 & L \\ -C_1 & 0 \end{bmatrix},$$
 (22)

where the variable  $s_1$  represents the state of the bi-directional DC-DC converter's top switch (either 1 or 0), and the number of possible states, n, in this case, is 2. The parameter  $C_1$  represents the capacitance on the DC bus side of the converter, while L corresponds to the converter's inductance.

Discretizing with the forward Euler method gives:

$$\mathbf{g}_{k+1} = \mathbf{A}_m \mathbf{m}_k - \mathbf{A}_d \mathbf{g}_k, \tag{23}$$

where  $A_m$  and  $A_q$  are the system matrices

$$\mathbf{A}_q = T_s \cdot \mathbf{H}^{-1} \cdot \mathbf{S} + \mathbf{I},\tag{24}$$

$$\mathbf{A}_m = T_s \cdot \mathbf{H}^{-1}. \tag{25}$$

The discretization simplifies the control implementation while maintaining the model's dynamic accuracy.

#### 325 2.4.3 Control of the generating machine DC-AC converter (G-C-AC)

The G-C-AC converter ensures the electrical machine tracks the commanded rotational speed regardless of load torque. A proportional-integral (PI) controller calculates the reference electromagnetic torque,  $T_{e_{ref}}$ , from the mechanical speed error, which is then used by the model predictive control (MPC)-MPC as a reference.

For the induction machine (IM), the MPC employs the discretized model seen in Sect. 2.4.2 and minimizes the normalized errors of the stator flux and torque, as shown in the cost function:

$$\mathcal{J} = \lambda_{\varphi} \cdot \frac{|||\overline{\varphi}_{s}|| - \varphi_{s_{\text{ref}}}|}{\varphi_{s_{\text{base}}}} + \lambda_{T} \cdot \frac{|T_{e} - T_{e_{\text{ref}}}|}{T_{e_{\text{base}}}},\tag{26}$$

where  $\lambda_{\varphi}$  and  $\lambda_T$  are weighting factors and  $\varphi_{s_{\mathrm{base}}}$  and  $T_{e_{\mathrm{base}}}$  are base values used for normalization.

For the permanent magnet synchronous generator (PMSG)PMSG, the MPC focuses on minimizing the torque error and reducing the *d*-axis stator current to enhance efficiency:

335 
$$\mathcal{J} = \lambda_i \cdot \frac{|i_{sd}|}{i_{s_{\text{base}}}} + \lambda_T \cdot \frac{|T_e - T_{e_{\text{ref}}}|}{T_{e_{\text{base}}}}.$$

where  $\lambda_i$  and  $\lambda_T$  are weighting factors and  $i_{s_{\text{base}}}$  and  $T_{e_{\text{base}}}$  are base values used for normalization.

Control diagrams for both machine types are shown in Fig. 7.

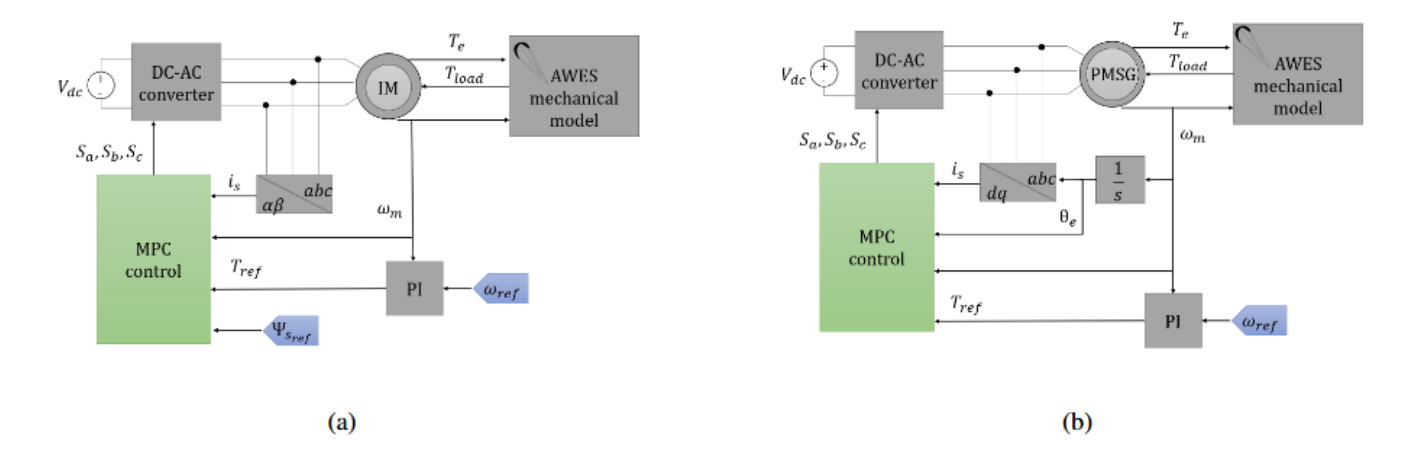


**Figure 7.** Control scheme schemes for the generator machine DC-AC converter (G-C-AC): (a) Control scheme when an induction machine is used, (b) Control scheme when a permanent magnet synchronous generator is used.

Control scheme for the generator machine DC-AC converter (G-C-AC) when a permanent magnet synchronous generator is used. Control schemes for the generator machine DC-AC converter (G-C-AC).

## 2.4.4 Control of the kite emulator machine DC-AC converter (K-C-AC)

The K-C-AC converter applies a reference torque to emulate the kite's mechanical behavior during the AWES cycle. This torque is computed using the single-mass mechanical model:

$$J_{\rm eq} \cdot \frac{d\omega_m}{dt} = T_e - T_{\rm load},\tag{28}$$

where  $J_{\text{eq}}$  is the equivalent inertia,  $T_e$  is the electromagnetic torque, and  $T_{\text{load}}$  is the load torque.

Similar to the G-C-AC, the MPC for the K-C-AC uses the machine's discretized model and minimizes reference variable errors according to Equation 26 for the IM and Eq. (27) for the PMSG. Control schemes for the IM and PMSG implementations are presented in Fig. 8.

#### 2.4.5 Control of the DC-DC converter

345

The DC-DC converter maintains a constant DC bus voltage by regulating power flow between the battery and the DC bus. The MPC uses measured currents and voltages to minimize the normalized errors in battery current ( $i_L$ ) and DC bus voltage ( $V_{dc}$ ) using the cost function:

350 
$$\mathcal{J} = \lambda_{i_L} \cdot \frac{|i_L - i_{L_{\text{ref}}}|}{i_{L_{\text{base}}}} + \lambda_v \cdot \frac{|V_{\text{dc}} - V_{\text{dc}_{\text{ref}}}|}{V_{\text{dc}_{\text{base}}}},$$
(29)

where  $\lambda_{i_L}$  and  $\lambda_v$  are weighting factors and  $V_{\text{dc}_{\text{base}}}$  and  $i_{L_{\text{base}}}$  are base values used for normalization. The control scheme for the DC-DC converter maintaining a stable DC bus is found in Fig. 9

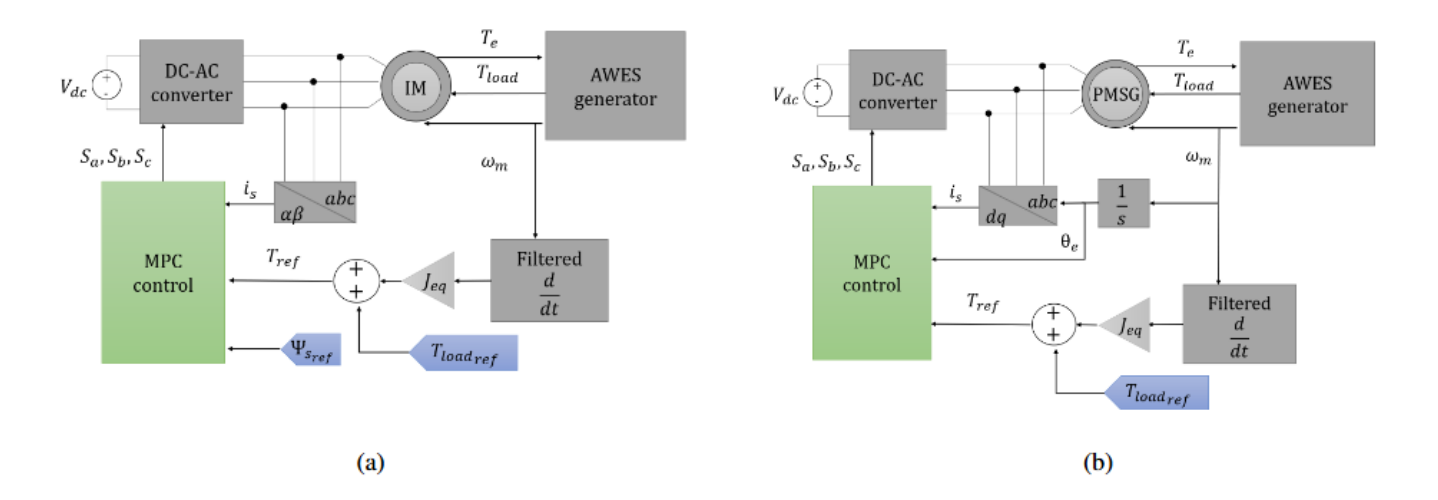


**Figure 8.** Control scheme schemes for the emulator machine DC-AC converter (K-C-AC): (a) Control scheme when an induction machine is used, (b) Control scheme when a permanent magnet synchronous generator is used.

Control scheme for the emulator machine DC-AC converter (K-C-AC) when a permanent magnet synchronous generator is used. Control schemes for the emulator machine DC-AC converter (K-C-AC).

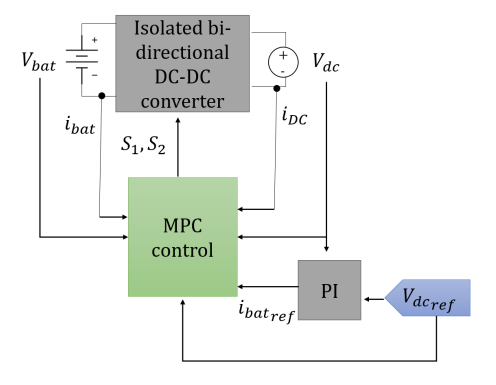


Figure 9. Control scheme for the DC-DC converter to maintain a steady DC bus voltage.

# 3 Proposed case study

365

To validate The validation of the AWES electric emulator topology and the proposed MPC control, real experimental flight data from a commercial AWES device, following an optimal mechanical path at an average wind speed of 7 m s<sup>-1</sup>, were used. These results validate the proposed emulator for AWES applications of similar characteristics. The recorded flight time series data for two cycles, including tether tension and tether length variation, were obtained from ?. These was carried out using two publicly available Kitepower flight datasets, as summarized in Table 1. Dataset 1 (Aruba) provides digitized time series of tether force and tether length for two AWES cycles recorded at Vader Piet Wind Farm in August 2021 (?). Dataset 2 (Leiden) contains raw measurements of tether force and tether speed for two AWES cycles recorded at the former Valkenburg airfield in October 2019 (?).

In both datasets, the recorded linear variables were translated into equivalent torque and rotational speed references reference signals for the emulator using the methodology described in Sect. 2.2, assuming a drum radius of  $R_{\text{drum}} = 0.3 \,\text{m.} R_{\text{drum}} = 0.2 \,\text{m.}$  This procedure ensures that the emulator operates under representative mechanical conditions derived from actual AWES operation, enabling a consistent evaluation of control performance across the two datasets.

**Table 1.** Summary of publicly available Kitepower datasets used in this study.

Parameter	Dataset 1 (Aruba)	Dataset 2 (Leiden)		
Location	Vader Piet Wind Farm, Aruba	Former airfield Valkenburg (Leiden, NL)		
Date	August 2021	8 October 2019		
Average wind speed	6.5 m/s	7.7 m/s		
Number of AWES cycles analyzed	2 cycles	2 cycles		
Kite type and technology	Falcon 100 kW test; leading-edge in- flatable kite; ground-gen	Inflatable flexible kite; ground-gen 100 kW prototype		
Kite area	60 m wing area <sup>2</sup>	Total 25 m <sup>2</sup> ; projected 19.76 m <sup>2</sup>		
Variables extracted	Tether force and tether length	Tether force and tether speed		
Data treatment	Digitized graphs to numerical data	Raw data imported directly		
Source	?	?		

# 3.1 Case study and test environment

375

380

390

395

Experimental—The evaluation was carried out in two stages using the mechanical profiles from ?, representing two AWES eyeles, were first tested on a real AWES generator (the two datasets summarized in Table 1. For each dataset, reference profiles of the optimum reel-out and reel-in speeds, together with the corresponding torque acting on the generator, were derived for two complete AWES cycles.

In the first stage, the mechanical-to-electrical power conversion system shown in Fig. ??) using the proposed MPC control for two electrical machines 4(a) was tested using these reference profiles. The generator was commanded to follow the optimum reel-out and reel-in speed profile from the dataset, while the electrical machine experienced the corresponding reference torque profile. This configuration was tested for two machine types: an induction machine (IM) and a permanent magnet synchronous generator (PMSG). Subsequently, the proposed AWES electrical test bench emulator topologies (.

In the second stage, the two emulator topologies shown in Figs. ?? and ??) were tested under the same control strategy and experimental data. 4(b) and 4(c) were evaluated using the same datasets. In these configurations, the generator machine was again commanded to follow the reference speed profile, while the emulator machine was torque-controlled to reproduce the reference torque profile corresponding to the AWES operation. Both IM and PMSG machines were considered for the test bench emulator, used in various combinations for the emulator tests. All analyses in both stages were repeated for each of the two datasets in order to enable consistent performance comparison across different operating conditions.

The tests were conducted in the MATLAB/Simulink environment, with all electrical hardware modeled using Simscape Electrical. Parameters for modeling and control are detailed in Appendix C.

# 3.2 Control objectives and performance indicators

385 The main objectives of the proposed MPC control, along with their corresponding performance metrics, are as follows:

- Accurate torque tracking with minimal ripple: Ensure that the kite emulator machine precisely follows the reference load torque of the AWES while minimizing electromagnetic torque ripple. Performance is evaluated using the normalized root mean squared error (RMSE) RMSE between the measured load torque on the shaft and the reference torque from the AWES dynamic profile.
- Precise speed regulation of the generator machine: Maintain accurate tracking of the optimal reference speed during both transient and steady-state operation. This is assessed using the normalized RMSE between the measured mechanical shaft speed and the reference speed from the AWES dynamic profile.
  - Maximization of energy conversion efficiency: Optimize the total electrical energy extracted from the available mechanical energy of the AWES cycle. Efficiency is quantified as the ratio of total energy stored in the battery to the total mechanical energy generated by the kite.
  - Stable and regulated DC bus voltage: Ensure a steady and well-regulated DC bus voltage throughout operation. This
    is evaluated using the normalized RMSE between the measured DC bus voltage and the reference voltage.

#### 4 Results

This section presents the performance evaluation of the proposed AWES test bench emulator for the two proposed datasets, highlighting its ability to replicate the dynamic behavior of a real AWES. Key numerical performance metrics are summarized in Tables Table 2 and 3. Experimental results for the kite emulator and generator dynamics are detailed in Fig. 10 Figs. 10 and 11, focusing on the torque, speed, and power profiles for two optimal figure-8 AWES cycles.

## 4.1 Numerical performance metrics

compares the

#### 405 **4.1.1 Dataset 1**

Table 2 summarizes the numerical performance metrics obtained when applying the mechanical profiles from Dataset 1 (Aruba). The table reports the overall and maximum energy efficiencies (η<sub>total</sub> and η<sub>max</sub>) for PMSG and IM machines, along with both generator types, as well as root mean square errors (RMSE) for speed, torque, and DC bus voltage. The table also includes battery performance metrics, such as In addition, battery performance is characterized by the number of AWES cycles required to charge or discharge the batteries for under both separated and common DC bus topologies. PMSG machines show The PMSG configuration achieves slightly higher efficiency, particularly during reel-in phases, while IM machines exhibit comparable accuracy in torque and speed tracking reel-in phases, whereas the IM configuration exhibits comparable tracking accuracy in speed and torque.

Table 2. Performance evaluation of AWES and test bench emulator for Dataset 1 (Aruba) across generator types and emulator topologies.

AWES				AWES test bench emulator								
			AWES cycles	Speed	Ratte	Battery	Torque	Speed	$V_{dc}$	AWES cycles	AWES cycles	AWES cycles
Generator	$\eta_{\mathrm{total}}$ (pu)	$\eta_{\mathrm{max}}$ (pu)	to charge	=	Emulator	topology	RMSE (%)	RMSE (%)	RMSE (%)	to charge	to discharge	to discharge
			G-B							G-B	K-B	J-B
					PMSG	Separated	0.44	0.6	0.11	563	390	-
PMSG	0.82	0.93	557	0.6		Common	0.43	0.6	0.15	-	-	1460
					IM	Separated	0.96	0.48	0.11	569	382	
						Common	0.94	0.48	0.14	-	-	1188
IM	0.78	0.91	586	0.04	IM	Separated	1.01	0.04	<del>0.1-</del> 0.10	596	382	-
1111	5.76				Common	0.97	0.05	0.13	-	-	1087	

#### 4.1.2 **Dataset 2**

415 A parallel evaluation was performed using the mechanical profiles from Dataset 2 (Leiden). The same performance indicators are reported in Table 3, following the structure used for Dataset 1. PMSG again demonstrates higher energy efficiency compared

to IM, while IM offers marginally improved speed tracking. Torque tracking errors are slightly higher for both machines compared with the results from Dataset 1, likely due to the more dynamic nature of this dataset. Overall, both configurations exhibit reduced global efficiency, as the operating points deviate further from the machines' nominal torque and speed ratings.

Table 3. Performance evaluation for Dataset 2 (Leiden) across generator types and emulator topologies.

AWES				AWES test bench emulator								
Generator	$\eta_{ m total}$ (pu)	$\eta_{ m max}$ (pu)	AWES cycles to charge G-B	Speed RMSE (%)	Emulator	Battery topology	Torque RMSE (%)	Speed RMSE (%)	V <sub>dc</sub> RMSE (%)	AWES cycles to charge G-B	AWES cycles to discharge K-B	AWES cycles to discharge J-B
					PMSG	Separated	0.5	0.82	0.14	415	161	
PMSG	0.6	0.88	385	0.81		Common	0.49	0.82	0.18	_	-	292
					<sub>IM</sub>	Separated	1.58	0.69	0.35	408	155	_
						Common	1.6	0.7	0.4	-	_	252
IM	0.42	0.82	555	0.07	IM	Separated	0.93	0.06	1	528	155	-
		-				Common	1	0.07	0.83	_	-	216

#### 420 4.2 Emulated mechanical dynamics

Figure 10 showcases

#### **4.2.1 Dataset 1**

425

430

435

Figure 10 illustrates the performance of the AWES emulator for two figure-8 cycles optimal figure-8 cycles when using PMSG machines for both the generator and kite emulator. Figure ?? highlights the kite emulator for Dataset 1. In Fig. 10(a), the torque applied by the emulator , accurately replicating closely reproduces the reference torque profile from the real AWES, with low ripple and high precision. Similarly, Fig. ?? demonstrates the generator's ability to track the accuracy. Figure 10(b) demonstrates that the generator tracks the commanded optimal rotational speed with less than a root mean square error below 1%RMSE. These. The results correspond to the case with separated DC buses; however, the torque and rotational separated DC bus configuration; the corresponding torque and speed profiles for the common DC bus configuration were found to be nearly identical, indicating that the bus topology has minimal impact on these influence on these dynamic variables.

# 4.2.2 **Dataset 2**

A parallel evaluation was conducted using the profiles from Dataset 2 (Leiden). Figure 11 follows the same layout as that used for Dataset 1 and illustrates the torque tracking, speed tracking, and filtered power readings. Similar to the results shown for Dataset 1, the proposed control strategy enables the emulator to closely reproduce the torque profile from the AWES with low ripple and high accuracy, while the generator accurately tracks the reference speed. As with Dataset 1, the torque and

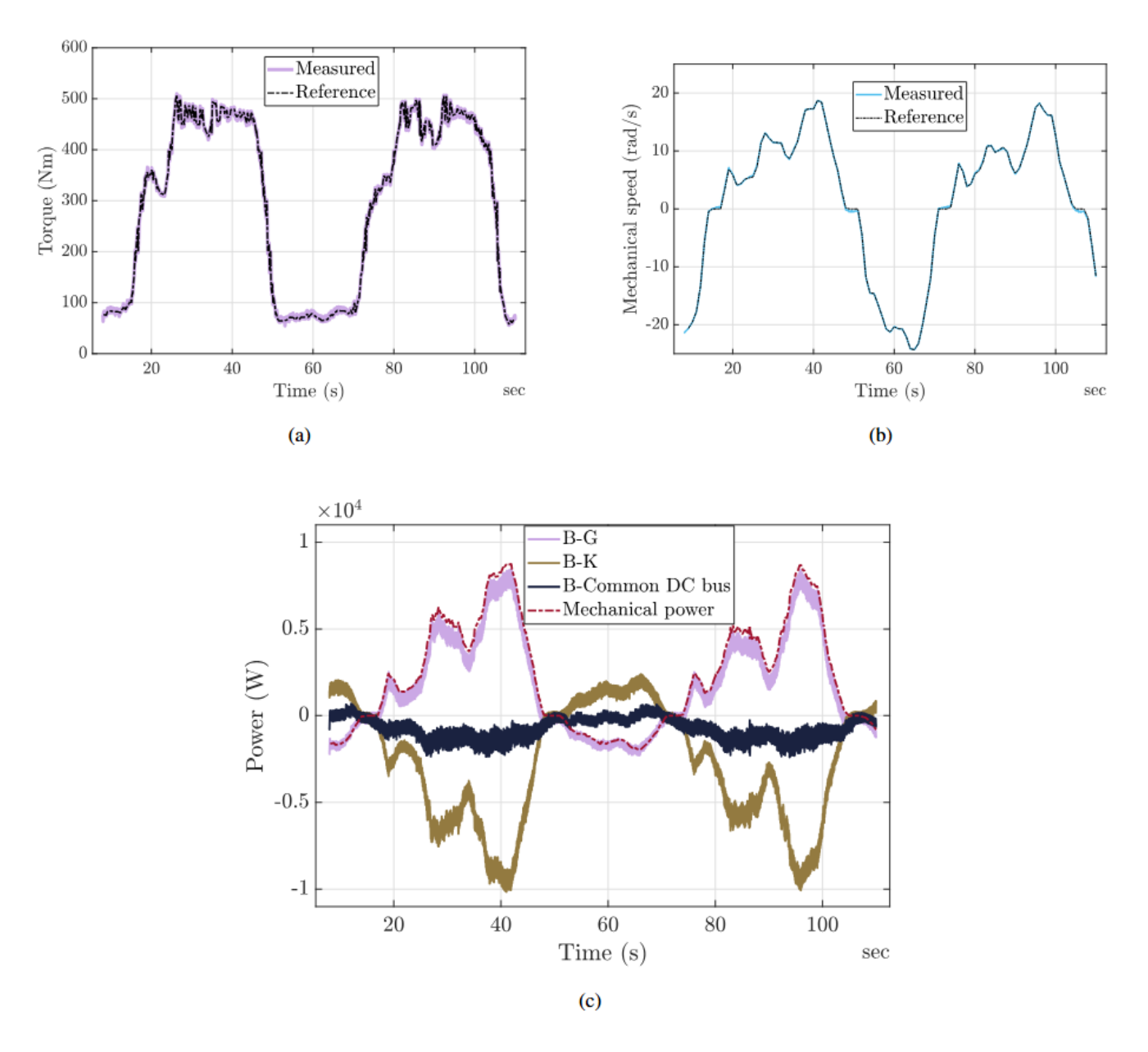


**Figure 10.** Case study results for two optimal figure-8 cycles of the AWES emulator using PMSG machines from Dataset 1 (Aruba): (a) Emulated kite torque, (b) Mechanical speed of the system, (c) Filtered power readings for the generator and emulator batteries.

speed profiles shown correspond to the separated DC bus configuration, since the results obtained with the common DC bus configuration were found to be nearly identical.

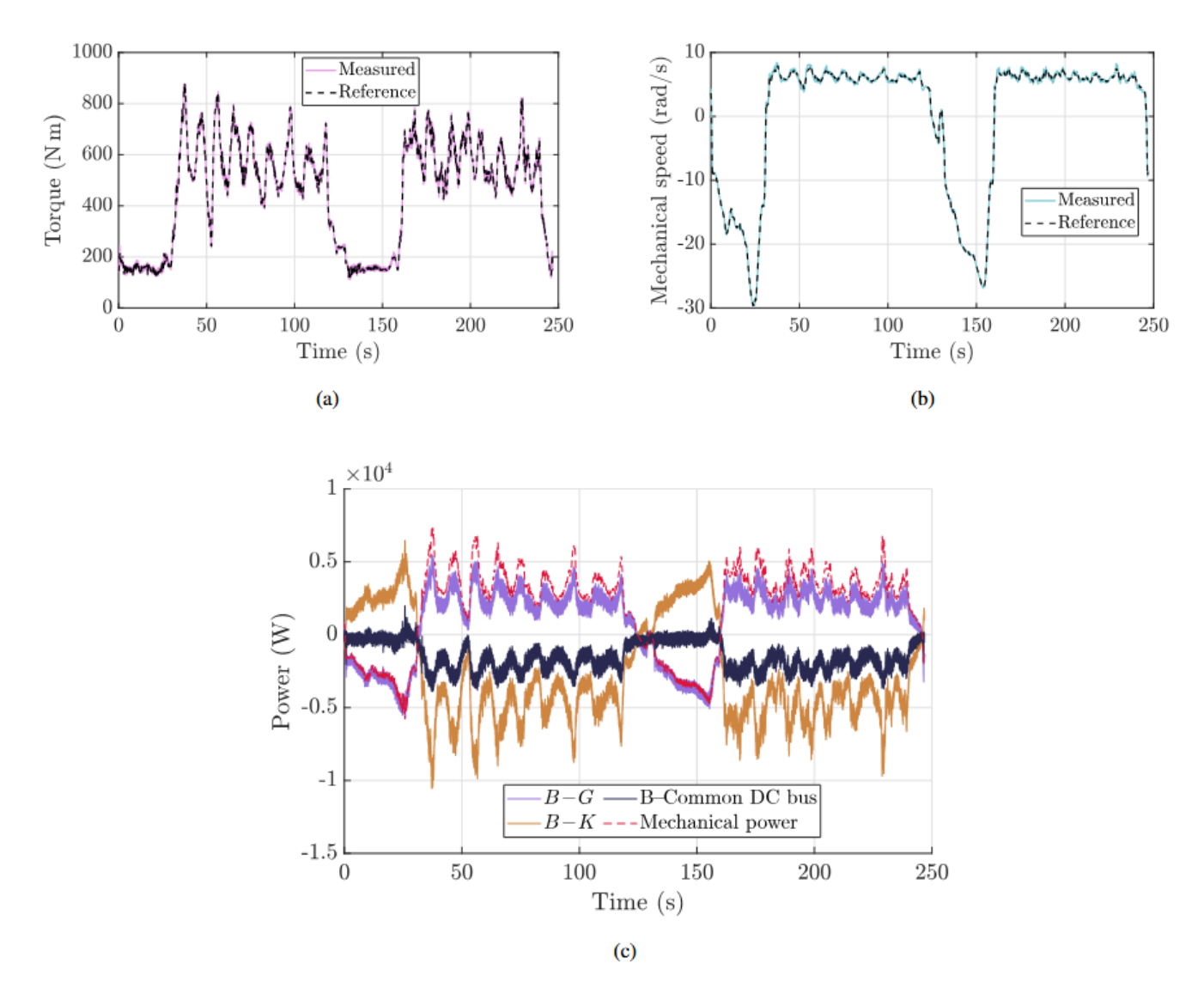


**Figure 11.** Case study results for two optimal figure-8 cycles of the AWES emulator using PMSG machines from Dataset 2 (Leiden): (a) Emulated kite torque, (b) Mechanical speed of the system, (c) Filtered power readings for the generator and emulator batteries.

## 4.3 Battery performance, power profiles and efficiency analysis

The filtered power profiles in Fig.?? compare the energetic performance of separated and common DC bus configurations

. The separated configuration shows distinct charging and discharging profiles for G-B 10 (c) highlight the fundamental differences between our two DC-bus configurations for Dataset 1. In the separated topology, the G-B and K-B, resembling the behavior of real AWES batteries. The K-B legs exhibit distinct charge and discharge waves, closely matching true AWES battery cycling. By contrast, the common DC bus configuration achieves significant power recirculation, reducing reliance on

the battery and enabling redirects most generated energy back into the machine emulator, yielding a near-zero net bus flow, so that under these test conditions the battery sees only small net transfers. This internal recirculation, for this dataset, reduces battery wear and delivers roughly 280–370% more AWES-cycles per charge, making it ideal for rapid, repeatable electric machine control-strategy tuning. It is not intended to mimic a real grid-tied system, where excess power would be exported via a grid-tie converter, but rather to offer a low-degradation test mode. For studies focused on realistic storage dynamics (for example battery sizing, round-trip efficiency, or state-of-charge effects) the separated-bus layout remains the preferred choice.

When the same evaluation is performed using Dataset 2 (see Fig. 11 (c), both electrical machines exhibit significantly lower global efficiency. This reduction is attributed to the operating points in Dataset 2 being further from the machines' nominal torque and speed regions, where electrical machines typically perform less efficiently. Under these conditions, the separated-bus topology remains the only configuration that accurately reproduces realistic storage dynamics. However, the common-bus topology still offers a reduced hardware requirement, using fewer converters and batteries, and—although the battery-cycling reduction is less pronounced than in Dataset 1, it continues to require fewer charge–discharge cycles than the separated-bus configuration. It therefore remains the preferred option for repeated test campaigns where only the emulation of electrical machine dynamics is relevant and storage behaviour is not under study.

To summarise these trade-offs and to make the discussion clearer for the reader, Table 4 provides a concise side-by-side comparison of both topologies. It highlights the hardware requirements, fidelity to actual AWES storage behaviour and machine dynamics, the efficiency-dependent battery cycling characteristics observed in both datasets, and the type of studies each configuration is best suited for. However, the separated topology is better suited for storage focused studies.

**Table 4.** Emulated kite torque Comparison of separated and common DC-bus configurations.

445

450

455

460

Mechanical speed of the system. Filtered power readings for the generator and emulator batteries. Case study results for two optimal figure. 8 cycles by the AWES emulator using PMSG machines.

Aspect	Separated DC Bus	Common DC Bus
DC-DC converters	2	1
Battery banks	2	1
Storage fidelity	High (≈98% real AWES storage)	Low (energy recirculated)
Dynamics fidelity	High	High
AWES cycles per charge/discharge	B-G similar to AWES, K-B $\simeq 50\%$ of G-B	Efficiency-dependent, always > B-K in separated
Best suited for	Storage & energy-management studies	Rapid control prototyping & machine-dynamics tests

Figure 12 provides 12 shows the instantaneous efficiency profiles of IM and PMSG machines during the generating (reel-out) phase of one AWES cycle. reel-out) phase for both datasets. In Dataset 1 (Fig. 12 (a), PMSG consistently outperforms IM at low power levels, with a maximum efficiency difference of about 6%. At higher power levels, both machines achieve similar efficiency reach similar efficiencies, with differences below 2%. For Dataset 2 (Fig. 12 (b), overall efficiencies for both machines are lower, consistent with operation at points further from their nominal ratings. The efficiency gap between PMSG and IM remains visible and is more pronounced, though still below 10%. An increase in power ripple also appears to affect partial efficiencies, contributing to the larger fluctuations seen in the efficiency profiles.

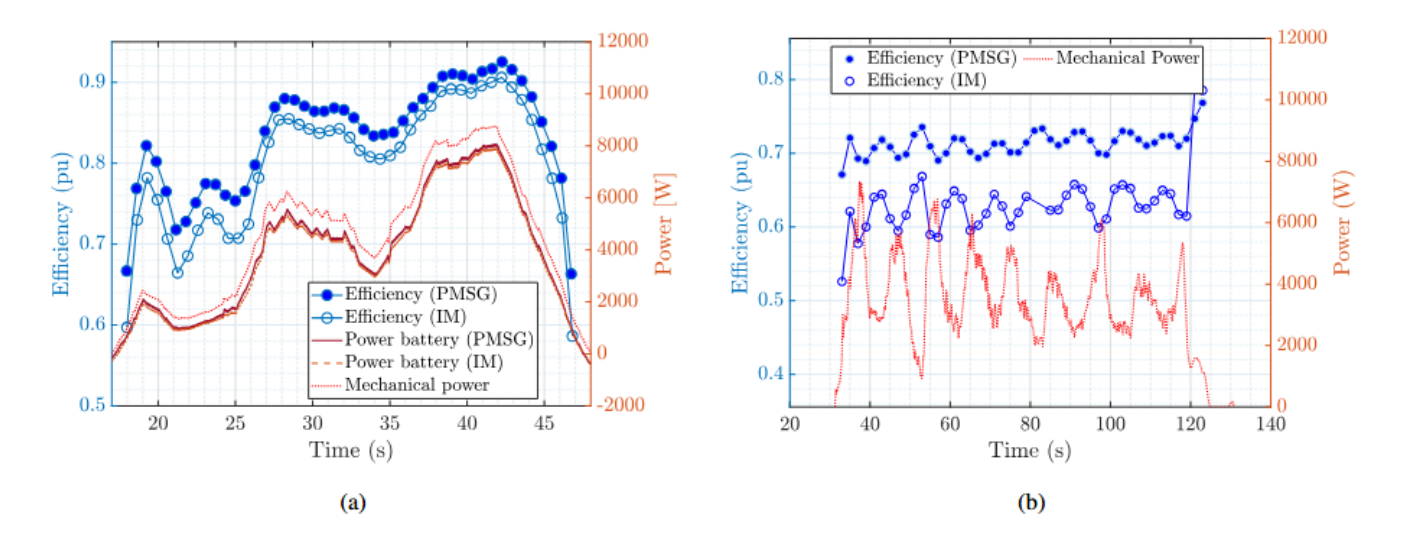


**Figure 12.** Instantaneous energy efficiency of the power conversion system during the generating phase of one AWES cycle: (a) For Dataset 1, (b) For Dataset 2.

#### 5 Conclusions

465

This paper presents a validated electric topology and torque ripple-optimizing model predictive control (MPC) ripple-optimizing MPC strategy for an airborne wind energy system (AWES) generator and its corresponding test bench electrical emulator. While extensive research has been conducted focused on optimizing AWES flight trajectories and aerodynamic performance, the mechanical-to-electrical mechanical-to-electrical power conversion process remains underexplored. This study addresses that gap by reviewing key AWES power conversion architectures and validating an efficient control framework that accurately emulates AWES energy dynamics using experimental data from two AWES flight cycles: Dataset 1 recorded in Aruba and Dataset 2 recorded in Leiden.

The proposed electric topology and MPC control effectively convert the mechanical energy extracted from an optimal AWES flight path into electrical energy, achieving a total system efficiency exceeding 80% across two complete flight cycles (reel-in

and reel-out) of 82% for Dataset 1 (Aruba) and 60% for Dataset 2 (Leiden), with maximum instantaneous efficiencies of 93% and 88%, respectively. The system maintains precise speed control, with the generator tracking the reference rotational speed within a 0.44% RMSE for Dataset 1 % root-mean-square error (RMSE). Both and 0.82% RMSE for Dataset 2, and the emulator tracks the reference torque with 0.11% and 0.14% RMSE, respectively. Across both datasets, permanent magnet synchronous generators (PMSG) and induction machines(IM) were evaluated as potential AWES generator options, with PMSG machines demonstrating superior performance, outperform induction machines, achieving 4% higher total energy efficiency and in Dataset 1 and an even larger—but still under 20%—efficiency gap in Dataset 2, with instantaneous efficiency improvements of 2–6% compared to IM machines. Both machines exhibit increasing efficiency at higher instantaneous power levels, with peak efficiencies reaching 93%, underscoring the importance of integrating electrical efficiency considerations into AWES flight path designin high-efficiency regions.

The test bench emulator presented in this paper accurately reproduces the mechanical dynamics and AWES accurately reproduces AWES mechanical dynamics, providing a controlled environment for evaluating power conversion and control strategies. The proposed torque ripple-optimized MPC ensures that the emulator machine follows the reference torque profile with an RMSE below 1%, effectively simulating the mechanical forces experienced by an AWES generator. While both PMSG and IM machines perform effectively in the emulator, IM machines exhibit slightly higher torque tracking errors (0.5%) and a 2% reduction in energy efficiency compared to PMSG machines. These results highlight the flexibility of the test bench to accommodate different machine types while maintaining precise control and energy conversion.

Two test bench topologies were analyzed: a separated DCbus topology, which closely mimics the energy storage behavior of real AWES ground stations, and a common DC bus topology, which significantly reduces battery requirements by facilitating direct energy recirculation between the generator and emulator machines. The separated DC bus topology achieves separated DC-bus topology achieves about 98% accuracy fidelity in replicating real AWES energy storage dynamics but requires 45–55% greater battery capacity for the emulator. The common DCbus topology, while less suited for energy storage studies, is highly effective for long-duration control tests, reducing battery dependency to just one-third of the , making it the preferred configuration when studying energy management or storage behavior. By contrast, the common DC-bus topology recirculates energy between the generator and emulator, reducing battery requirements by roughly two-thirds. Although it does not reproduce detailed storage operation, it enables long-duration, repeated machine-dynamics tests with minimal battery cycling.

Across both datasets, operating the electrical machines outside their nominal region results in a degradation of AWES cycle efficiency, highlighting the critical importance of proper machine dimensioning. Reduced conversion efficiency in off-nominal regions drives significantly higher battery cycling even under a common-bus setup. Nevertheless, if, and only if, storage dynamics are not under study and only machine dynamics are required, the common-bus configuration is the most cost-effective solution, using less hardware and imposing lower peak discharge stresses than the separated configuration.

The findings in this study These findings highlight the effectiveness and versatility of the proposed AWES power conversion strategies and emulator. By filling bridging a gap in AWES research, this work provides a foundation for integrating mechanical and electrical efficiency considerations into AWES system design, making it highly relevant not only for power system researchers but also for those specializing in AWES aerodynamics to both power system and flight control researchers.

Future work should focus on eo-optimizing co-optimizing flight trajectories and power conversion strategies, exploring efficiency gains at varying power levels, and expanding the test bench framework to support grid integration and larger-scale larger-scale AWES applications. In addition, the proposed control strategy should be benchmarked against alternative control approaches to further validate its relative performance. Experimental validation is also required to strengthen and build upon the design conclusions presented here. Finally, when detailed ground-station models become available, incorporating a more specific mechanical model to estimate rotational variables from tether length and speed data would enhance the fidelity of the emulator and improve the applicability of the results.

Author contributions. Conceptualization, D.S. and C.N; methodology, C.N., D.S, F.D. and J.G.; software, C.N..; validation, C.N.; formal analysis, C.N and F.D.; investigation, C.N.; resources, D.S..; data curation, C.N and J.G.; writing—original draft preparation, C.N. and F.D.; writing—review and editing, C.N., F.D., D.S. and J.G.; visualization, C.N., D.S, F.D. and J.G; supervision, D.S.; project administration, D.S. All authors have read and agreed to the published version of the manuscript.

525 Competing interests. The authors declare no competing interests.

Acknowledgements. This work is part of the project PID2022-141520OB-I00 funded by MICIU/AEI/ 10.13039/501100011033. Work by F.D.-N. was supported by the grant with reference IND2022/AMB-23521 funded by Comunidad de Madrid. AI tools have been used exclusively to proofread and format specific parts of the manuscript.

## Appendix A: Values for induction motor model matrices using a static reference frame

The following matrices define the state-space representation of the induction motor (IM) model in a stationary reference frame. In these matrices,  $R_s$  and  $R_r$  represent the stator and rotor resistances, respectively, while  $L_s$ ,  $L_r$ , and  $L_m$  denote the stator, rotor, and magnetizing inductances. The parameter  $\omega_e$  corresponds to the electrical angular speed of the rotor.

$$\mathbf{A} = \begin{bmatrix} 0 & R_s \\ 0 & 0 \end{bmatrix}, \qquad \mathbf{B} = \begin{bmatrix} 0 & 0 \\ -j\omega_e & R_r \end{bmatrix}, \qquad \mathbf{C} = \begin{bmatrix} 1 & 0 \\ 0 & 0 \end{bmatrix},$$

$$\mathbf{D} = \begin{bmatrix} 0 & 0 \\ 1 & 0 \end{bmatrix}, \qquad \mathbf{E} = \begin{bmatrix} \frac{L_r}{L_m} & \frac{L_m^2 - L_r L_s}{L_m} \\ \frac{1}{L_m} & -\frac{L_s}{L_m} \end{bmatrix}. \tag{A1}$$

## 535 Appendix B: Values for the PMSG model matrices using a dq reference frame

The following matrices describe the state-space representation of the Permanent Magnet Synchronous Generator (PMSG) PMSG model in a rotating dq reference frame. Here,  $R_s$  represents the stator resistance, while  $L_d$  and  $L_q$  correspond to the direct-axis and quadrature-axis inductances. The parameter  $\omega_e$  denotes the electrical angular speed of the rotor.

$$\mathbf{F} = \begin{bmatrix} R_s & -L_d \omega_e \\ L_q \omega_e & R_s \end{bmatrix}, \qquad \mathbf{G} = \begin{bmatrix} 0 & -\omega_e \\ \omega_e & 0 \end{bmatrix}, \qquad \mathbf{L} = \begin{bmatrix} L_d & 0 \\ 0 & L_q \end{bmatrix}.$$
 (B1)

# 540 Appendix C: Case Study Parameters

This section summarizes the key electrical and control parameters used in the case study, including battery specifications, converter characteristics, and machine properties. These values define the operational limits and dynamic behavior of the AWES test bench emulator.

<b>Battery Parameter</b>	Value
Nominal voltage $(V_{nom})$	360 V
Internal resistance $(R_{bat})$	$0.1~\Omega$
Usable energy	14.76 kWh

Table C1. Battery parameters.

The PMSG and IM parameters used in this study (see Table C3) were adapted from well-established designs for 10–30 kW class wind-energy machines, which align with those implemented in early AWES prototypes and laboratory test benches?. Ground-generation systems such as the Ampyx 12 kW and TU Delft 20 kW platforms demonstrate similar operating ranges and machine characteristics, supporting their suitability for emulating AWES dynamics. These parameters are consistent with

DC-DC Converter Parameter	Value
Capacitance 1 $(C_1)$	$4.7 \cdot 10^{-4} \text{ F}$
Capacitance 2 $(C_2)$	$1 \cdot 10^{-4} \text{ F}$
Inductance $(L)$	$1.4\cdot 10^{-3}~\mathrm{H}$
Resistance 1 $(R_1)$	$1\cdot 10^{-3}~\Omega$
Resistance 2 $(R_2)$	$1\cdot 10^{-3}~\Omega$
Switching frequency $(f_{switch})$	10 kHz

**Table C2.** DC-DC converter parameters.

IM Parameter	s	PMSG Parameters			
Moment of inertia $(J_{eq})$	$2.5\mathrm{kg\cdot m^2}$	Moment of inertia $(J_{eq})$	$2.72\mathrm{kg\cdot m^2}$		
Pole pairs (p)	8	Pole pairs (p)	8		
Leakage inductance $(L_{lr})$	0.1931 pu	$d/q$ inductance $(L_d, L_q)$	$15\cdot 10^{-3}~\mathrm{H}$		
Leakage inductance $(L_{ls})$	0.1316 pu	Flux linkage $(\varphi_m)$	0.85 Wb		
Mutual inductance $(L_m)$	5.3833 pu	Stator resistance $(R_s)$	$0.2~\Omega$		
Rotor resistance $(R_r)$	0.0658 pu	Nominal power $(P_n)$	20 kW		
Stator resistance $(R_s)$	0.0302 pu	Nominal voltage $(V_n)$	380 V		
Nominal power $(P_n)$	20 kW				
Nominal voltage $(V_n)$	380 V				

**Table C3.** Parameters for induction machine (IM) and permanent magnet synchronous generator(PMSG).

values reported in wind-energy literature for machines of comparable scale ?, ensuring the emulator reflects realistic hardware while allowing future updates as more AWES-specific data become available.

Control DC-DC Paramet	ters	Control DC-AC Parameters		
Integral gain $(K_i)$	45	Integral gain $(K_i)$	200	
Proportional gain $(K_p)$	1	Proportional gain $(K_p)$	250	
Cost weight $(\lambda_{i_L})$	1	Cost weights	$\lambda_i = 1, \lambda_T = 1$	
Switching frequency $(f_{switch})$	10 kHz		$\lambda_{\varphi} = 2, \lambda_T = 1$	

Table C4. Control parameters for DC-DC and DC-AC converters.